Tectonophysics 846 (2023) 229653

Contents lists available at ScienceDirect

Tectonophysics

journal homepage: www.elsevier.com/locate/tecto

Spatially varying crustal stress along the Zagros seismic belt inferred from earthquake focal mechanisms

Ahad Nouri [a], Behnam Rahimi [a,*], Václav Vavryčuk [b,c], Farzin Ghaemi [a]

[a] Department of Geology, Faculty of Sciences, Ferdowsi University of Mashhad, Azadi Sq., Mashhad, Khorasan Razavi, Iran
[b] Institute of Geophysics, Czech Academy of Sciences, Boční II/1401, 14100 Praha 4, Czech Republic
[c] Institute of Geology, Czech Academy of Sciences, Rozvojová 269, 16500 Praha 6, Czech Republic

ARTICLE INFO

Keywords:
Zagros
Tectonic stress
Stress inversion
Earthquake
Focal mechanism

ABSTRACT

We determine the stress field of the Zagros fold-and-thrust belt (ZFTB) in the collisional zone between the Arabian and Iranian plates. Using 898 mainshock focal mechanisms, which occurred along the belt between 1956 and 2021, we calculate stress at 32 locations. The results reveal that the crustal stress in the Zagros belt is heterogeneous with variations in the orientation of SH_{max} as well as in the stress ratio. The interpolation of the Simpson's index $A\phi$ points to three distinct domains: northern, central and southern, which are characterized by wrench, compressional, and wrench-compressional to compressional tectonic regimes, respectively. Tectonic stress in the study area is characterized by a horizontal to sub-horizontal maximum compression axis in the ~NE-SW to ~NNW-SSE direction. The GPS measurements of the strain tensor and the SH_{max} direction inferred from the stress inversion indicate that both the deformation pattern and the seismicity along the ZFTB zone are primarily affected by convergence of the Arabian and Iranian plates.

1. Introduction

The Zagros fold-and-thrust-belt (ZFTB) lies in the collision zone of the Arabian and Iranian plates (Fig. 1). The Iranian plate is an assembly of continental fragments and small narrow oceanic or sub-oceanic basins. This plate is separated from adjacent plates by belts of basement faults known as the ZFTB to the west, the Alborz-Kopeh Dagh fold-and-thrust belt to the north, Makran subduction zone to the south, and Eastern Iranian range as a result of the India-Eurasia collisional to the east (Bagheri and Gol, 2020; Berberian and King, 1981; Stern et al., 2021). The ZFTB covers southwest and west of Iran, north of Iraq, and south of Turkey in the NW-SE direction. The region is an active fold-and-thrust belt that results from the northeast-dipping subduction below the Iranian micro-continent and the subsequent collision (e.g., Berberian and King, 1981; Koshnaw et al., 2021; Stern et al., 2021; Zebari et al., 2021). After the collision due to NE-SW directed shortening resulted from the oblique convergence between the Arabian and Iranian plates, the sedimentary cover of the basement warped into NW-SE-trending folds and thrusts. Consequently, the belt underwent thickening and shortening from Late Cretaceous-Early Paleocene time (Berberian and King, 1981; Berberian, 1995). As a result of continuous shortening, a southward migration of the deformation front over the basement has happened until now (Zebari et al., 2021), leading the belt to achieve ~300 km in width. According to McQuarrie et al. (2003), the direction of convergence changed from ~30°N (67.7 Ma) to ~5°N (10.6 Ma). Recent GPS measurements carried out along the ZFTB (Khorrami et al., 2019) show that the convergence currently varies from ~19 mm/yr at 48°E to ~27 mm/yr at 58°E with respect to the Eurasia-fixed reference frame. The rate of current shortening across the belt varies along strike of the zone, decreasing from ~9 ± 2 mm/yr at ~54°E to 4 ± 2 mm/yr at ~47°E in a roughly north-south direction (Vernant et al., 2004).

The Arabian-Iranian plate convergence-derived deformation is accommodated by both longitudinal NW-SE-trending contractional structures and intermountain strike-slip faults (Talebian and Jackson, 2002; Allen et al., 2004; McQuarrie, 2004; Doski, 2021; Zebari et al., 2021). The northern boundary of the belts is marked by the Main Zagros oblique thrust fault (MZOTF) accommodating most of the strike-slip movement across the region (Talebian and Jackson, 2002). Based on the geological and geomorphological studies carried out along the MZOTF (Talebian and Jackson, 2002), the right-lateral offset along the MZOTF is ~50 km. Recently, studies on the northern side of the ZFTB (Niassarifard et al., 2021) reveal that another basement fault branching from MZOTF participates in accommodation of the strike-slip movements. The fault transfers the strike-slip movements to NW Iran-SE

* Corresponding author at: Department of Geology, Faculty of Sciences, Ferdowsi University of Mashhad, Azadi Square, Mashhad, Khorasan Razavi, Iran.
E-mail address: b-rahimi@um.ac.ir (B. Rahimi).

https://doi.org/10.1016/j.tecto.2022.229653
Received 27 December 2021; Received in revised form 26 October 2022; Accepted 10 November 2022
Available online 24 November 2022

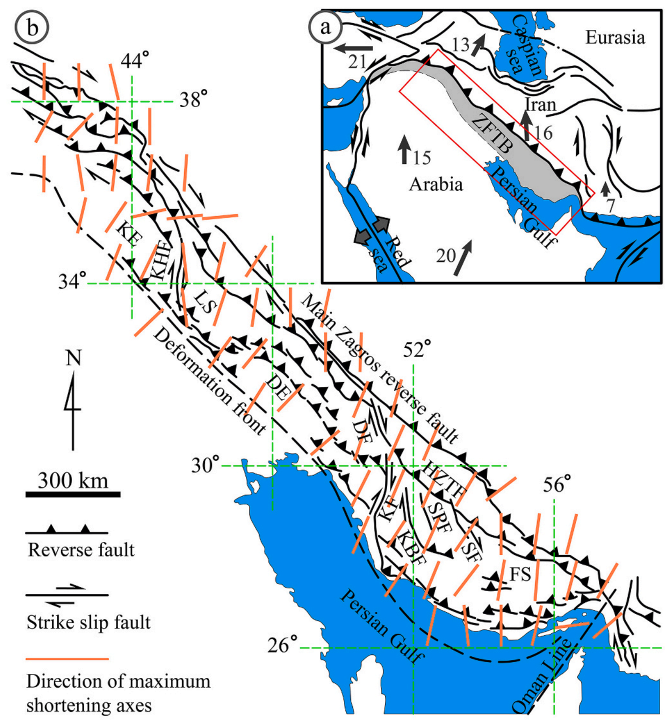

Fig. 1. Tectonic map of the Arabian-Eurasian collision zone and the Zagros fold-and-thrust belt (ZFTB) (after Berberian, 2014). (a) Location of the study area (red rectangle) in the geodynamic framework of the Arabian-Eurasian collision zone (Reilinger et al., 2006; Vernant et al., 2004). Black arrows and numbers represent the GPS-derived plate velocities (mm/yr) relative to Eurasia (Reilinger et al., 2006). (b) Simplified fault map of the ZFTB. (Berberian, 2014). HZTF: High Zagros thrust fault, SPS: Sabz-Pushan fault, SF: Sarvestan fault, KBF: Kar-e-bas fault, KF: Kazerun fault, DF: Dena fault, KHF: Khanqin fault, FS: Fars salient, DE: Dezful embayment, LS: Lurestan salient, and KE: Kirkuk Embayment. Directions of the maximum shortening axes were deduced from the GPS measurements (Khorrami et al., 2019). (For interpretation of the references to color in this figure legend, the reader is referred to the web version of this article).

Turkey. According to balanced cross-sections across the ZFTB (McQuarrie, 2004), the belt achieves in total 70 ± 20 km shortening, corresponding to ~20% convergence between the Arabian and Iranian plates.

Seismically, the Zagros belt is one of the most active zones in the region. Most of the seismic activity of the belt is concentrated near the basal detachment (Talebian and Jackson, 2002) decoupling the sediments and basement (Berberian and King, 1981; Berberian, 1995). The majority of the large earthquakes in the Zagros belt are generated by the reactivation of range parallel oblique reverse basement faults and transverse strike-slip fault systems, while small earthquakes take place within the sedimentary succession covering the crystalline basement (Jackson, 1980; Berberian, 1995). Although a large number of moderate (M 5–6) earthquakes occurred in the ZFTB, the Ezgeleh Sarpolzahab earthquake (2017/11/12, Mw 7.3) is the largest instrumentally recorded earthquake in the belt (Nissen et al., 2019).

One of the keys to understanding the complex tectonic behavior in the area is knowledge of tectonic stress. In contrast to the structural framework of the ZFTB, which is rather well known (e.g., Berberian, 1995; Talebian and Jackson, 2002; Alavi, 2007; Navabpour et al., 2008; Doski, 2021; Niassarifard et al., 2021; Zebari et al., 2021), details about tectonic stress and the SH_{max} in the belt are still undisclosed. Various studies carried out to determine the present-day stress in the ZFTB using the earthquake focal mechanisms (EFM) were focused on isolated focal zones only (e.g. the Kazerun, Kar-e-bas, and Sabz-Pushan fault zones in south east of Zagros). Although they did not study the stress pattern for the whole ZFTB, they indicated that tectonic stress might be heterogeneous (e.g., Navabpour et al., 2008; Sarkarinejad et al., 2018; Nouri Mokhoori et al., 2021; Aflaki and Mousavi, 2021). By contrast, Ghorbani Rostam et al. (2018) analyzed stress in the southern part of the ZFTB (latitude <30°N) and concluded that no significant stress variation is detected within the area.

Since the spatial variation of tectonic stress is important for better understanding the active faulting pattern and the processes responsible for earthquakes (e.g., Levandowski et al., 2018; Scholz, 2019; Snee and Zoback, 2020), the aim of this paper is to provide the stress pattern for the whole ZFTB zone. Our study area covers over 2000 km of the ZFTB, extending from Oman Line to south of Turkey (Fig. 1). Specifically, we aim to address the following three objectives: (1) the spatial variation of the orientation of the principal stress axes along the ZFTB, (2) the spatial variation of relative magnitudes of the principal stress axes in terms of the Simpson's index $A\phi$ representing the stress regime (Simpson, 1997), and (3) the trajectory pattern of the SH_{max} orientation across the belt. Finally, we discuss the stress and faulting map of the Zagros belt in the context of the structural and geodynamic pattern of the region.

2. Tectonic and geological setting

The NW-SE-trending Zagros fold-and-thrust belt marks the northern margin of the Arabian plate, extending from the Oman line in the southern Iran to SE Turkey (Alavi, 2007; Stern et al., 2021). The belt is a result of closure of the Neotethys ocean and contains a thick succession of sediments, ranging in age from the latest Precambrian to recent time (Alavi, 2004). Rifting through Zagros during the Permo-Triassic time caused Iran to move away from the NE African-Arabian plate and produced Neotethys Ocean (Berberian and King, 1981; Koshnaw et al., 2021; Stern et al., 2021). The suggested time the subduction of the Neotethys Ocean crust beneath Iran varies from ~200 Ma to ~100 Ma. The subduction, which lasted until Cenozoic was accompanied by the Late Cretaceous and Cenozoic volcanism (Stern et al., 2021). The time of the collision between the Iranian and Arabian plates is not well known and varies from Upper Cretaceous (Cenomanian-Maastrichtian) to Oligocene–Miocene (Cai et al., 2021; Koshnaw et al., 2021; Stern et al., 2021). After the collision, the crust of the Zagros has undergone to shortening (thrusting and folding) and the modern tectonic regime of the region was produced.

Seismically, the MZOTF exhibits the north eastern abrupt depth-dependent cut-off of seismic activity of the Zagros seismic belt (Berberian, 1995; Jackson, 1980). The seismicity of the Zagros occurs on high angle (up to 60°) reverse faults. This is thought to indicate faulting in the Zagros may take place on inherited rifting-related early Mesozoic normal faults, which have subsequently been reactivated as thrust faults (Jackson, 1980; Jackson and Fitch, 1981; Jackson and McKenzie, 1984). These faults follow a local trend of the belt at the surface (Berberian, 1981; Jackson and McKenzie, 1984). Although seismicity in the Zagros defines a NE-dipping thrust to oblique faulting, geodetic studies (Roustaei et al., 2010) have revealed that the S-dipping reverse faulting also occurs within the belt. In addition to these, a series of ~N-S-trending strike-slip faults in the south western part of the Zagros accommodate right-lateral movements (Berberian, 1981; Jackson and McKenzie, 1984; Talebian and Jackson, 2004).

The sedimentary cover of the ZFTB consists of evaporitic units, like the lower Cambrian Hormoz Salt and the salt rich mid-Miocene Gachsaran formation that would act as detachment horizons. Thickness and repetition of these units within the sedimentary column of the Zagros make it unlikely that there is a simple correlation between basement and surface structures (Jackson, 1980; Berberian, 1995; Jackson and McKenzie, 1984; McQuarrie, 2004; Alavi, 2004, 2007). Evaporate horizons prevent fault propagation from the basement toward the surface. Such faulting deforms the sediments by folding (Berberian, 1981, 1995; Jackson and McKenzie, 1984; Nissen et al., 2007).

Structurally, the southern part of the region is more complicated.

Fault strikes and fold axes achieve progressively the ~E-W orientation toward the Oman line, and thrust fault systems are interconnected with tectonically active strike-slip faults. The faults mostly show dominant thrust faulting with a strike-slip component. The deformation through the domain is without any partitioning along the MZOTF collisional plate boundary (Berberian, 1995; Vernant et al., 2004; Vernant and Chéry, 2006). McQuarrie (2004) believed that the existence or non-existence of the Hormoz salt in the southern and central domains controls the large-scale structures in the region. According to McQuarrie (2004), the existence of the Hormoz salt in the sedimentary column of the southern domain allows to generate the folds independently from the basement over the Hormoz Salt, while due to the absence of the Hormoz salt in the central domain, contractional structures dominantly appear as dense thrust faulting.

Toward north, the Arabian-Eurasian convergence is partitioned into the thrust faulting through the Greater Caucasus and right-lateral movements through north of Iraq, northwest of Iran and southeast Turkey (Jackson, 1992). The strike-slip fault zone transfers the northward motion-derived deformation of the Arabian plate to the East and North Anatolian fault zone (Jackson, 1992; Talebian and Jackson, 2002; Khorrami et al., 2019; Niassarifard et al., 2021).

3. Data and method

In this study, publicly available EFM data from two different sources were used: (1) online networks that report the focal mechanisms of earthquakes, like the Global Centroid Moment Tensor (CMT) catalogue, and (2) published documents, like Talebian and Jackson (2004), Jackson and McKenzie (1984), and Rebetsky et al. (2017). Following Soh et al. (2018), we filtered the data according to the two rules: (1) Small-magnitude earthquakes ($M < 2.5$) were not considered because they might represent deformation owing to the complex interaction of faults rather than the deformation resulted from the regional stress field. This is often the case for foreshocks and aftershocks (Zoback, 1992; Heidbach et al., 2018; Soh et al., 2018). (2) Since large-magnitude earthquakes would generate spatial and temporal perturbations in stress (Stein, 1999; Hardebeck and Okada, 2018), we selected mainshocks by using the method proposed by Reasenberg (1985) that could represent the background stress field in the study area. As a result, the final data set comprises 898 EFMs with magnitudes ranging from 2.5 to 7.2 that took place between 1956 and 30 July 2021 (Supplementary data). The magnitude of 13.5% earthquakes ranged from 2.5 to 3.9, mainly concentrated in three subsets (7, 19 and 32). Using the Frohlich's (1992) classification method, the focal mechanisms mostly show thrust to strike-slip faulting (Fig. 2).

The EFM data set was subdivided into subsets through two steps. First, the data were subdivided into K clusters using the k-means clustering algorithm (Aggarwal, 2014), see Fig. 3 for a location of clusters. The k-means clustering algorithm classifies n earthquakes to K clusters regardless of the data similarity and/or associated structural domains of

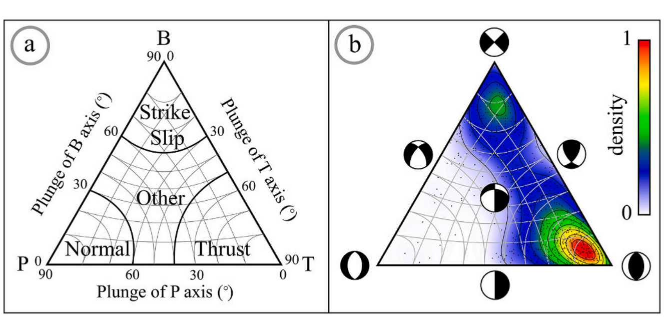

Fig. 2. (a) Classification of the focal mechanisms as a function of the plunge angle of the P, B, and T axes in the Frohlich triangular diagram (Frohlich, 1992). (b) Distribution of focal mechanisms on the Frohlich diagram.

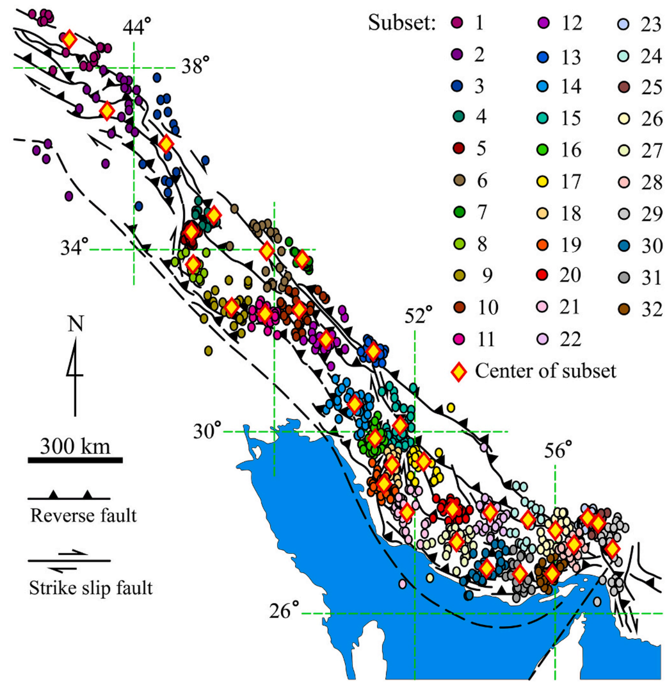

Fig. 3. Distribution of epicenters of earthquakes with EFMs on the fault map of ZFTB. Colors refer to different clusters. Centers of clusters are also indicated.

the earthquakes, but it ensures that each earthquake is assigned to a cluster, which has a nearest center to the earthquake epicenter. Second, based on the associated structural domain and the similarity of the EFMs, the datum/data of the adjacent clusters was/were added to a cluster that contains similar data. In the stress analysis, the number of clusters are determined based on an optimum required number of focal mechanisms to constrain a stable stress, associated structural domain of mechanisms, earthquake density, and an average deviation angle of the calculated stress (e.g. Abolfathian et al., 2020; Martínez-Garzón et al., 2016; Townend et al., 2012). This strategy was repeated for several times until the best-fit stress tensor of each subgroup, containing at least 15 EFMs (Michael et al., 1990), finds the smallest possible average misfit angle α. The misfit angle defines the angular difference between the observed and theoretically determined slip directions. This angle served as an indicator of homogeneity of the stress field (Michael et al., 1990; Martínez-Garzón et al., 2016): the homogeneous stress was considered for $\alpha \leq 35^\circ$ (Michael, 1991).

To determine the stress (directions of three principal stress axes and their relative magnitude) from the EFM data, we used the iterative joint inversion for stress and fault orientations proposed by Vavryčuk (2014). Since incorrectly selected fault planes can bias the retrieved stress ratio (Vavryčuk, 2015), the method uses the fault instability parameter I to select which of nodal planes corresponds to the correct fault plane (Vavryčuk, 2011, 2014; Vavryčuk et al., 2013). The instability parameter I is defined as:

$$I = \frac{\tau - \mu(\sigma - 1)}{\mu + \sqrt{1 + \mu^2}} \tag{1}$$

where τ is the shear traction along a fault plane, μ is the fault friction, and σ is the effective normal traction (compression is assumed positive). The correct fault plane is that which has the higher fault instability (where $0 \leq I \leq 1$). Indeed, this method quantifies which nodal plane is nearest to the optimal orientation for the slip according to the Mohr-Coulomb failure criterion. However, the heterogeneity of the crust might complicate the problem. The best-fit stress tensor is calculated in several iterations: (1) directions of the principal stress axes and their relative magnitudes are determined using the Michael's method

(Michael, 1987) with initially randomly selected nodal planes as the faults, (2) the correct fault planes are identified by the fault instability criterion, and (3) the step (1) with newly defined faults and step (2) are repeated on a grid of friction values to maximize the overall fault instability. Finally, the resultant stress is determined by using the most unstable nodal planes identified through the iterations.

To classify the tectonic regime across the study area, we used the Simpson's index $A\phi$ (Simpson, 1997). This index ranges in the interval between 0 and 3 and defines the tectonic regime as follows: $A\phi = 0$ - radial extensional, $A\phi = 0.5$ - extensional, $A\phi = 1.5$ - wrench, $A\phi = 2.5$ - compressional, and $A\phi = 3$ - pure compressional tectonic regime. The value of index $A\phi$ is given by:

$$A\phi = (n + 0.5) + (-1)^n\ (\phi – 0.5) \tag{2}$$

where ϕ is the stress ratio

$$\phi = (\sigma_2 - \sigma_3)/(\sigma_1 - \sigma_3) \tag{3}$$

and $n = 0$, 1 and 2 for the extensional, wrench and compressional tectonic regimes, respectively.

Once directions of the SH_{max} are calculated for each stress state using the method proposed by Lund and Townend (2007), the SH_{max} trajectory map is drawn over the whole area using the distance-weighting method proposed by Lee and Angelier (1994).

4. Results

Applying the abovementioned method, we subdivided the dataset of 898 EFMs into 32 subsets with an average of ~28 focal mechanisms per subset (Fig. 3). According to numerical modeling performed by Vavryčuk (2015), the number of focal mechanisms used in each subset should be sufficient for an accurate determination of stress. The results of the stress inversion carried out on the 32 subsets are listed in Table 1 and shown in Fig. 4.

The average misfit deviation angle α calculated for each subset is <35° (Table 1, Fig. 5a). Hence, according to the above mentioned criteria (Michael, 1991), the stress can be considered as homogeneous within all subsets. Nevertheless, when we compare individual subsets, the angle α considerably varies. This points to a different degree of the stress homogeneity or a different quality of EFMs of individual subsets. The highest value of α is 32.7° for subset 3. It also has the lowest number of EFMs. It might point to some local stress complexities in the area covered by this subset. Some of the variability can come from noise in data. To eliminate the effect of noise on the judgment of the homogeneity/heterogeneity of stress, we applied the Michael's (Michael, 1991) assumption. According to Michael (1991), assuming the error of focal mechanisms of about 10° - 20°, the homogeneous stress field is satisfied when the average deviation angle α is less than ~35°.

Throughout the study area, stress axis σ_1 is horizontal or sub-horizontal (the plunge values vary from 0° to 15°), with the exception of subset 23, which shows a plunge of 22° (Table 1). The value of stress ratio ϕ varies from 0.02 to 0.51 (Table 1, Fig. 5b) and indicates that the relative magnitudes of the σ_2 and σ_3 are mostly rather close each to the other. For 19 of 32 subsets, the stress ratio ϕ is even smaller than 0.2 (Table 1), which implies that the relative magnitudes of the σ_2 and σ_3 are very close and they can be interchanged (Pascal, 2021). Besides, the 95% confidence areas of the σ_1 axis of all stress states are tight. For most of subsets, the error in the σ_1 axis is about ±5°only (Fig. 4). Exceptionally, the error achieves a value of ±10° (subsets 12, 14, 25 and 31). In several cases, the σ_2 and σ_3 axes overlap and spread along strikes of each other. This applies, for example, to subsets 13 and 23 in Fig. 4. The overlap of the σ_2 and σ_3 axes indicates: (1) the presence of both wrench

Table 1
Stress state determined from focal mechanism data. The retrieved stress is represented by the orientation of the principal stress axes σ_1, σ_2, and σ_3 given by the trend/plunge (°) angles and by the stress ratio ϕ. Notation: n_S is the subset number, N is the number of EFMs of the subset used for stress state determination, α is the misfit angle (°), and $A\phi$ is the Simpson's index. Lat. and Lon. refer to the latitude and longitude of the center of each subset, and N, C, and S mean a northern, central and southern domain for each subset.

n_S	Domain	N	Lat. (°N)	Lon. (°E)	σ_1	σ_2	σ_3	ϕ	α (°)	$A\phi$	SH_{max} (°)
1	N	16	36.61	42.17	348/00	080/84	258/06	0.19	15.25	1.81	168
2	N	24	37.04	43.24	191/05	330/83	101/04	0.37	21.62	1.63	011
3	N	15	36.32	44.92	196/15	068/67	291/18	0.48	32.74	1.52	018
4	N	24	34.75	46.28	239/00	149/54	329/36	0.14	19.65	1.86	059
5	N-C	36	34.38	45.64	244/00	337/83	154/07	0.05	9.65	1.95	064
6	N	21	33.96	47.79	197/14	045/75	289/07	0.12	18.25	1.88	017
7	N	21	33.78	48.80	183/14	038/73	275/09	0.39	27.87	1.61	004
8	N-C	20	33.66	45.70	234/04	324/03	087/85	0.04	10.55	2.04	054
9	C	27	32.72	46.80	220/10	311/07	078/78	0.37	14.36	2.37	039
10	C	25	32.68	48.71	200/05	110/08	323/81	0.21	16.62	2.21	020
11	C	24	32.58	47.76	206/08	300/23	099/66	0.12	15.67	2.12	026
12	C	21	32.01	49.47	208/10	299/04	052/79	0.5	21.44	2.5	027
13	S-C	21	31.78	50.82	187/13	289/42	084/45	0.03	22.30	2.02	008
14	C	37	30.60	50.29	190/08	280/04	035/81	0.51	25.93	2.51	009
15	S-C	43	30.12	51.58	207/10	332/73	115/14	0.12	19.27	1.88	027
16	S-C	32	29.84	50.86	218/05	126.19	322/70	0.07	12.82	2.07	038
17	S-C	25	29.33	52.26	029/02	130/80	299/10	0.24	18.88	1.76	029
18	S-C	30	29.27	51.37	233/09	326/19	119/69	0.06	20.80	2.06	053
19	S-C	47	28.84	51.11	229/01	320/23	136/67	0.02	19.16	2.02	049
20	S	26	28.30	53.06	211/09	120/06	356/80	0.09	14.58	2.09	031
21	S-C	33	28.22	51.78	043/01	313/01	188/89	0.21	17.19	2.21	043
22	S	36	28.21	54.13	201/06	291/07	073/81	0.28	15.05	2.28	021
23	S	27	28.10	26.89	186/22	308/52	083/29	0.04	12.96	1.96	006
24	S	22	28.07	55.21	179/04	088/14	284/75	0.18	12.46	2.18	179
25	S	16	27.98	57.20	181/15	089/06	340/74	0.44	24.74	2.44	002
26	S	22	27.83	56.01	189/06	098/10	309/79	0.13	17.10	2.13	009
27	S	38	27.58	53.18	207/03	117/06	323/84	0.23	12.72	2.23	027
28	S	29	27.49	56.51	176/03	266/03	042/86	0.19	21.32	2.19	176
29	S	35	27.42	57.61	210/04	118/24	309/66	0.04	20.80	2.04	030
30	S	32	27.00	54.04	017/06	111/32	278/57	0.05	16.45	2.05	017
31	S	20	26.88	54.97	010/09	278/11	138/75	0.41	19.51	2.41	011
32	S	53	26.88	55.89	184/06	093/11	300/77	0.13	16.91	2.13	004

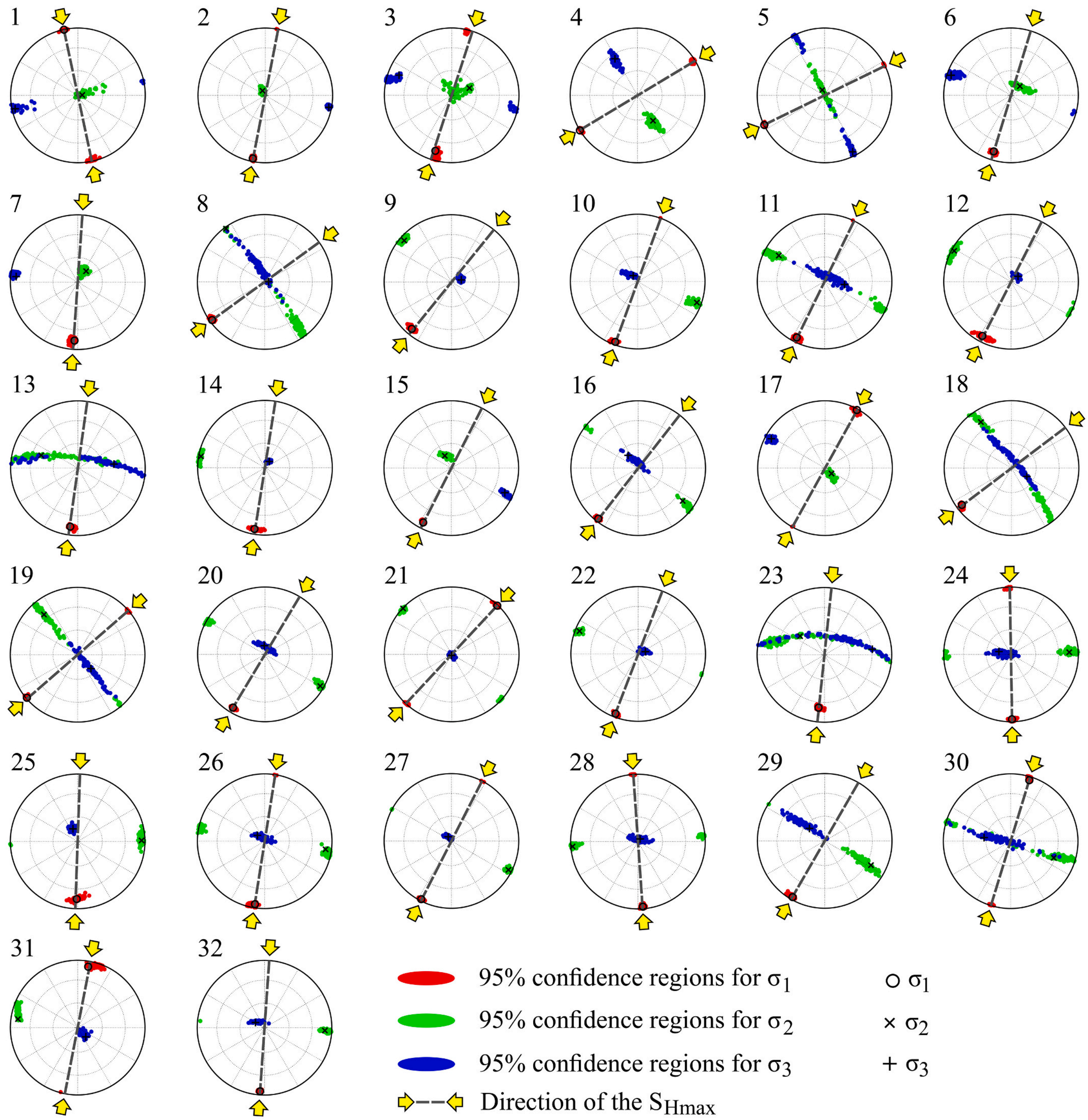

Fig. 4. Stress inversion results of 32 EFM subsets shown in Fig. 3. The subset number is indicated in the upper-left corner of each stereonet. For details, see the legend. Note that the σ_1 axis, which controls the SH_{max} direction, is well defined for most of subsets with the error of about ±5°.

to compressional tectonic regime ($A\phi = 1.52$ to 2.51) (Table, 1), and (2) the SH_{max} direction is roughly equal to the σ_1 axis (Lund and Townend, 2007; Vavryčuk, 2015).

The study area is characterized by a spatial variation of the tectonic regime from compressional through wrench-compressional to wrench regime, in which the minimum or the intermediate principal stress axis is (sub)vertical and the other two are (sub)horizontal (Fig. 4 and Table 1). The wrench tectonic regime takes place in the northwest of the study area, and also is observed along the MZOTF around 34°N, where deformation partitioning is evident (Talebian and Jackson, 2002; Walpersdorf et al., 2006; Khorrami et al., 2019). Toward the south of the ZFTB, the stress in the Fars and Lurestan regions is predominantly under the wrench-compressional regime with a tendency toward the compressional regime, while the Kazerun, Kar-e-bas fault zones are characterized by the wrench-compressional tectonic regime (Fig. 6). This points to complex tectonic processes, associated with different deformation types across the region.

Along the ZFTB, the direction of the SH_{max} displays lateral variations. The SH_{max} orientation varies appreciably from the ~NE-SW to ~WNW-ESE direction (Fig. 4 and Table 1). The SH_{max} trajectories in northwest of the study area are ~N-S, while they follow the ~NNE direction to the south (Fig. 6). The uncertainty of the SH_{max} depends mostly on the

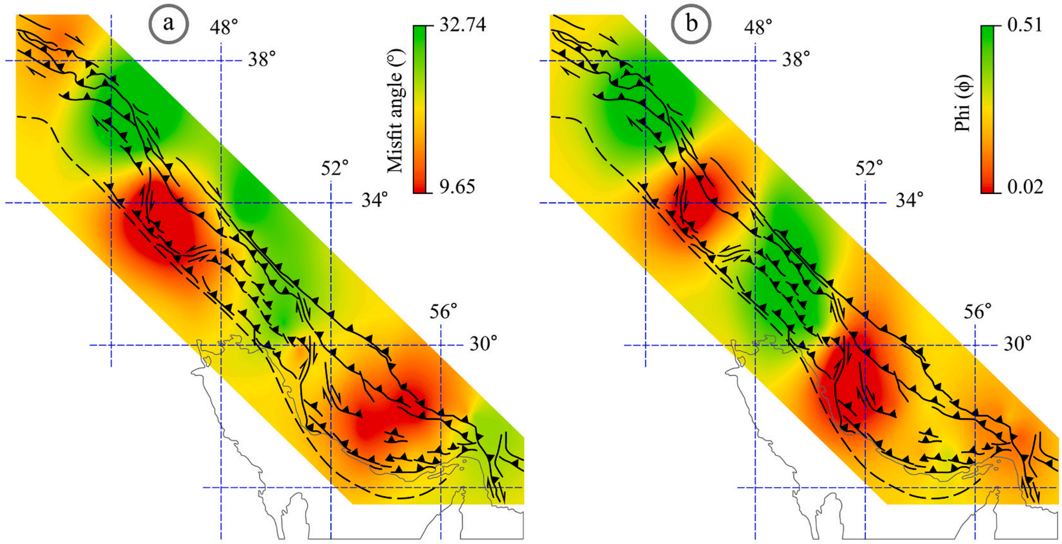

Fig. 5. Spatial variation of the misfit angle (a) and the stress ratio ϕ (b).

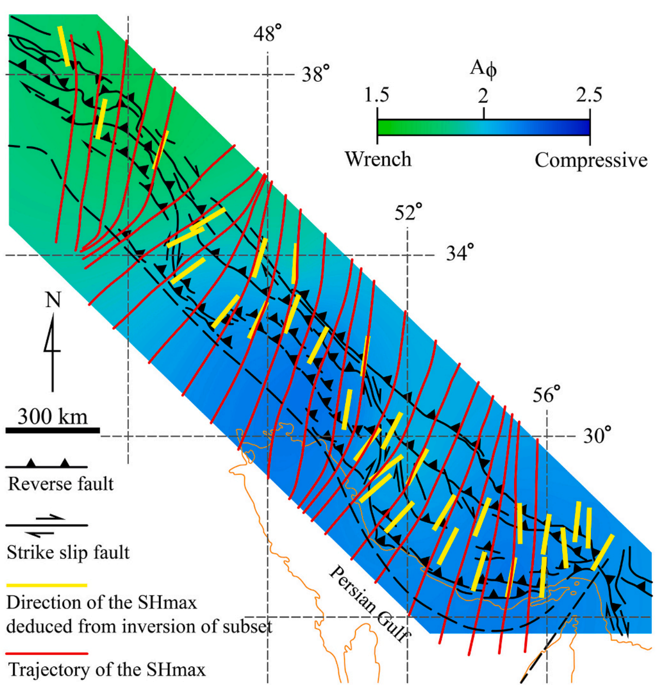

Fig. 6. The SH_{max} trajectories across the ZFTB on the map of the active stress regime of the belt. The type of the stress regime is color-coded.

uncertainty of the retrieved σ_1 principal stress direction, which is roughly horizontal. Since σ_1 is quite stable and well defined in individual cells with the error mostly <5° (see Fig. 4), the variation of the σ_1 direction and of the SH_{max} should not be considerably affected by noise in data.

5. Discussion

Interpolation of the $A\phi$ values (Fig. 6) reveals significant lateral variations of tectonic regime through the area. According to the variation of the $A\phi$ values, three domains can be distinguished for the Zagros belt (Fig. 6): the southern, central and northern domains. The tectonic regime across the southern and central domains has approximately a similar character. The regime is wrench-compressional in both southern and central domains having a tendency toward the compressional regime. Faulting in these domains is mostly thrusting in combination with strike slips. This suggests a prevailingly compressional regime. The stress regime in the central domain tends to be more compressional than that in the southern domain. The northern domain, where subsets 1, 2, 3, 4. 6, and 7 are characterized by the $A\phi$ values of 1.81, 1.63, 1.52, 1.86, 1.88 and 1.61, respectively, displays the wrench tectonic regime and the strike-slip type of faulting. The wrench regime of this domain suggests that the convergence between the Arabian and Eurasian plates in this domain transfers through the strike-slip faults to the south and southeast of Turkey by dominant right-lateral movements (Jackson, 1992; Talebian and Jackson, 2002; Niassarifard et al., 2021; Nouri Mokhoori et al., 2021). These domains are separated by transitional zones with the wrench-compressional tectonic regime. The southern zone of Zagros is defined by latitudes <34°N and it covers the Kazerun and Kar-e-Bass fault zones. In other words, the oblique convergence along the ZFTB leads to a dextral transpression through inherited fault zones in the ZFTB (Berberian, 1995; Alavi, 2007).

The ~N-trending Kazerun and Kar-e-Bass faults play a key role in transferring the lateral movement in southeast of Zagros (Berberian, 1995; Khorrami et al., 2019; Tavakoli et al., 2008; Walpersdorf et al., 2006) causing a low seismic activity of the north (~30°N) of the Kazerun and Kar-e-Bass faults. The low seismicity of the area can be justified by two different scenarios: (1) faults lying in this site are inactive at present (Talebian and Jackson, 2004), and (2) the deformation of this area transfers by the Dena, Kazerun, Kar-e-bas, and Sabz Pushan fault zones (Fig. 1) to the southern front of the ZFTB. The slip along these faults accommodates at a rate of 3.7, 3.6, 3.4, and 1.5 mm/yr, respectively. This process prevents the area from a high seismic activity (Tavakoli et al., 2008).

The variation of the tectonic regime through ZFTB may result from the angular difference between the convergence direction of the Arabian and Iranian plates and the collisional plate boundary, MZOTF. The convergence takes place at an angle of ~60° to trend of the ZFTB near the Oman Line. The angle decreases to ~35° toward north (Vernant and Chéry, 2006; Khorrami et al., 2019). Therefore, the convergence would resolve into two components: one is at a right angle to the ZFTB trend causing the compressional regime and the other is parallel to the ZFTB trend causing right-lateral movements. As evident by seismic and geodetic studies, this leads to deformation partitioning by strike-slip faulting along the northern border of the belt, the MZOTF, and thrust faulting along the NW-*SE*-trending faults within the belt (Talebian and Jackson, 2002; Talebian and Jackson, 2004; Walpersdorf et al., 2006;

Khorrami et al., 2019). Such a model was suggested for deformation partitioning through the central domain (Talebian and Jackson, 2004; Walpersdorf et al., 2006; Navabpour et al., 2008; Khorrami et al., 2019). However, this model is challenged by numerical modeling of the oblique convergence (Vernant and Chéry, 2006) that reveals that partitioning cannot take place completely in the Zagros belt, unless the collision between the Arabian and Iranian plates being very oblique. According to Vernant and Chéry (2006), MZOTF can accommodate ~25% of the whole tangential motion, implying that other processes can contribute to the accomodation of the deformation in this part of the belt.

The GPS measurements (Khorrami et al., 2019) reveal an extension along the ZRF between the Zagros and the Sanandaj-Sirjan zone, where the strike-slip movements are expected. Also, geological and geomorphological studies along MZOTF show evidence of ~N-S normal fault scarps (Talebian and Jackson, 2002, 2004). Such extension is not supported by our stress inversion results. Talebian and Jackson (2002, 2004) interpreted the extension as subsidiary to strike-slip faulting being confirmed by recent structural study carried out in the region (Niassarifard et al., 2021).

The SH_{max} orientation, tectonic regime, and stress ratio determined in this study are different from those of Navabpour et al. (2008) in the Kermanshah area, between latitudes 32.5°N and 37°N. Navabpour et al. (2008) determined the active stress state by using 31 EFM data. The authors subdivided the data into two subsets. Subset 1 contained 13 mechanisms located along the MZOTF, and subset 2 contained 18 mechanisms located within the belt. Navabpour et al. (2008) obtained the SH_{max} direction of N178°E for subset 1 belonging to a strike-slip regime ($A\phi = 1.47$) and N35°E for subset 2 belonging to a compressional regime ($A\phi = 2.45$). In this study, the stress state for this area was determined using 9 subsets, including clusters 3, 4, 5, 6, 7, 8, 9, 10, and 11 with an average of ~24 mechanisms per subset. Except for subsets 3 and 7 belonging to the wrench regime through MZOTF with N18°E and N4°E SH_{max}, respectively, and subset 9 associating with the compressional regime with N39°E SH_{max}, the stress analysis shows a dominant wrench-compressional regime ($A\phi = 1.86$–2.21) with the SH_{max} around N17°E to N64°E.

Sarkarinejad et al. (2018) carried out the stress inversion on 7 EFMs located along the Kar-e-Bass fault zone. According to Sarkarinejad et al. (2018), an extensional-wrench stress regime ($A\phi = 1.28$) with the N25°E-directed SH_{max} affects this fault zone. In our study, the center of subsets 17, 20, and 21 are placed along the Kar-e-Bass fault. The mechanisms located in subset 17 represent a N29°E SH_{max} belonging to a wrench-compressional tectonic regime with tendency to the wrench regime ($A\phi = 1.76$). The inversion of subset 20 indicates a wrench-compressional tectonic regime ($A\phi = 2.09$) with N31°E-directed SH_{max}. The inversion of subset 21 shows a N43°E-directed SH_{max} belonging to a wrench-compressional tectonic regime with tendency to the compressional regime ($A\phi = 2.21$). Hence, our results do not confirm the extensional-wrench tectonic regime proposed by Sarkarinejad et al. (2018).

The SH_{max} across the ZFTB is directed between N0°E and N64°E with an average of N23°E trend, as presented in Fig. 6 and Table 1. Since the SH_{max} is mainly controlled by the σ_1 axis, which is tightly constrained (see Fig. 4), the error of the SH_{max} is about ±5° only for most of subsets. Generally, the calculated directions of the SH_{max} are sub-parallel to the principal axis of the maximum horizontal contractional strain tensor inferred from GPS measurements (Khorrami et al., 2019). An exception is observed around 34°N, 46°E. The SH_{max} direction inferred from subsets 4, 5, and 8 show major disagreements, where the area marks a transition between the wrench-compressional tectonic regime to the south and the wrench regime to the north (Fig. 6). The deviation between the axes of the SH_{max} and the maximum horizontal contractional strain tensor can have several reasons: (1) the deformation partitioning takes place on preexisting weak planes on faults (Pourbeyranvand, 2018), (2) strain releases at 45° from the fault and through the slip direction of the faults with small shear strength, regardless of the spatio-temporal change of the stress direction (Gillard et al., 1996), (3) the transferring seismic activity through divers faults. When the seismic activity transfers from one to another fault, the direction of strain release will change, while direction of stress remain the same (Gillard et al., 1996), and (4) seismic indicators of the stress state (EFM data) would be represent a long-term stress tensor.

As shown in Fig. 6, the SH_{max} trajectories derived from the stress inversion are rotated counterclockwise through the belt from the southern part toward the northern part of the ZFTB. The orientation of the SH_{max} determined in this study is consistent with the orientation of the maximum contractional axis derived from the GPS measurement across the Zagros belt (Khorrami et al., 2019). This confirms a high accuracy of the determined direction of SH_{max}. Furthermore, this shows that both earthquakes and ground deformation patterns are linked to the same deep crustal stresses.

From the Oman line toward the southwest Zagros (30°N), the SH_{max} direction shows a change in orientation roughly following the orientation perpendicular to the deformation front (Fig. 6). The GPS measurements (Khorrami et al., 2019; Walpersdorf et al., 2006) show that the deformation in the southern part of Zagros is perpendicular to the ZFTB and restricted to the Persian Gulf shore. The similarity of our results compared to that of the GPS measurements (Walpersdorf et al., 2006; Khorrami et al., 2019) may indicate that the strain above the decollement and stress below it have similar axes.

Recently, Ranjbar-Karami et al. (2019) calculated the SH_{max} orientation in the Persian Gulf, south of Zagros. The authors used the in-situ stress determination and their results are fairly consistent with those presented in our study. Obviously, we cannot expect a perfect fit for several reasons: (1) The SH_{max} direction in this study was inferred from the EFM data mostly at depths ≥5 km (>95%), while the in-situ stress was determined at shallow depths <5 km. (2) The deformation across the stratigraphic column of the study area may be different with depth, due to decoupling the sedimentary units through detachment layers (Berberian, 1995; McQuarrie, 2004). (3) The measurements of the in-situ stress represent more likely local rather than regional stress.

Toward the northern part of the study area, where the strike-slip faulting of north of Iraq and southeast of Turkey occurs, the direction of the SH_{max} trajectories is changed and the trajectories become aligned in ~N-S.

6. Conclusions

The stress inversion from 898 earthquake focal mechanisms, which covered the Zagros fold-and-thrust belt zone, provides a stress pattern along the belt. The results show that the present-day stress across the ZFTB is not homogeneous but it displays spatial variations. The determined stress is characterized by a horizontal to sub-horizontal maximum stress axis σ_1. In most cases (19 of 32 subsets), a low value of the stress ratio (< 0.2) allows to interchange the σ_2 and σ_3 stress axes. Consequently, the tectonic regime varies from wrench to compressional along the belt and is consistent with the structural framework and the GPS measurements in the area. The northern, central and southern parts of the study area are characterized by the wrench, compressional and compressional to wrench-compressional regimes, respectively. The orientation of the SH_{max} deduced from the stress varies spatially through the belt from ~NE-SW to ~NNW-SSE. The calculated SH_{max} orientation is consistent with that of the maximum contractional axis of the strain tensor obtained from the GPS measurements. This indicates that both the active seismicity and deformation pattern of the region are driven by a deep crustal stress field related to the convergence between the Arabian and Iranian plates.

Credit author statement

Ahad Nouri: Conception and design of study, Acquisition of data, Software, Interpretation, Writing/editing/drafting/ revising the manuscript.

Behnam Rahimi: Conception and design of study, Interpretation, editing the manuscript.

Václav Vavryčuk: Interpretation, reviewing/editing the manuscript.

Farzin Ghaemi: Interpretation.

Declaration of Competing Interest

The authors declare that they have no known competing financial interests or personal relationships that could have appeared to influence the work reported in this paper.

Data availability

Data will be made available on request.

Acknowledgements

We thank the editor and two anonymous reviewers for their constructive and detailed reviews, which helped us to improve the paper considerably. This study was conducted as a part of the postdoctoral position project of the first author (A. N.) at the Ferdowsi University of Mashhad. One of co-authors (VV) was supported by the Czech Science Foundation, Grant No. 22-10747S. The inversion for stress was performed by the public-open Matlab code STRESSINVERSE developed by Vavryčuk (2014) (http://www.ig.cas.cz/stress-inverse), and plotting of the earthquake focal mechanisms on the Frohlich's diagram was performed by Orient software developed by Dr. Vollmer (http://www.frederickvollmer.com/orient/index.html).

Appendix A. Supplementary data

Supplementary data to this article can be found online at https://doi.org/10.1016/j.tecto.2022.229653.

References

Abolfathian, N., Martínez-Garzón, P., Ben-Zion, Y., 2020. Variations of stress parameters in the Southern California plate boundary around the South Central Transverse Ranges. J. Geophys. Res. Solid Earth 125 e2020JB019482.

Aflaki, M., Mousavi, Z., 2021. Interaction between the far-field stress and crustal boundary faults in the kinematics of active deformation around the Lut Block, Eastern Iran. Tectonophysics 817, 229053.

Aggarwal, C.C.A.R., 2014. Data Clustering: Algorithms and Applications. Chapman and Hall/CRC, Boca Raton, p. 652.

Alavi, M., 2004. Regional stratigraphy of the Zagros fold-thrust belt of Iran and its proforeland evolution. Am. J. Sci. 304, 1–20.

Alavi, M., 2007. Structures of the Zagros fold-thrust belt in Iran. Am. J. Sci. 307, 1064–1095.

Allen, M., Jackson, J., Walker, R., 2004. Late Cenozoic reorganization of the Arabia-Eurasia collision and the comparison of short-term and long-term deformation rates. Tectonics 23.

Bagheri, S., Gol, S.D., 2020. The eastern Iranian orocline. Earth Sci. Rev. 210, 103322.

Berberian, M., 1981. Active faulting and tectonics of Iran. Zagros Hindu Kush Himalaya Geodynamic Evolution 3, 33–69.

Berberian, M., 1995. Master "blind" thrust faults hidden under the Zagros folds: active basement tectonics and surface morphotectonics. Tectonophysics 241, 193–224.

Berberian, M., 2014. Earthquakes and Coseismic Surface Faulting on the Iranian Plateau. Elsevier, 628 p.

Berberian, M., King, G., 1981. Towards a paleogeography and tectonic evolution of Iran. Can. J. Earth Sci. 18, 210–265.

Cai, F., Ding, L., Wang, H., Laskowski, A.K., Zhang, L., Zhang, B., Mohammadi, A., Li, J., Song, P., Li, Z., 2021. Configuration and timing of collision between Arabia and Eurasia in the Zagros collision zone, Fars, southern Iran. Tectonics 40 e2021TC006762.

Doski, J.A., 2021. Active tectonics along the Sheladiz seismogenic fault in the Western Zagros fold-thrust belt, Kurdistan, Northern Iraq. Int. J. Earth Sci. 110, 595–608.

Frohlich, C., 1992. Triangle diagrams: ternary graphs to display similarity and diversity of earthquake focal mechanisms. Phys. Earth Planet. Inter. 75, 193–198.

Ghorbani Rostam, G., Pakzad, M., Mirzaei, N., Sakhaei, S.R., 2018. Analysis of the stress field and strain rate in Zagros-Makran transition zone. J. Seismol. 22, 287–301.

Gillard, D., Wyss, M., Okubo, P., 1996. Type of faulting and orientation of stress and strain as a function of space and time in Kilauea's south flank, Hawaii. J. Geophys. Res. Solid Earth 101, 16025–16042.

Hardebeck, J.L., Okada, T., 2018. Temporal stress changes caused by earthquakes: a review. J. Geophys. Res. Solid Earth 123, 1350–1365.

Heidbach, O., Rajabi, M., Cui, X., Fuchs, K., Müller, B., Reinecker, J., Reiter, K., Tingay, M., Wenzel, F., Xie, F., 2018. The World stress Map database release 2016: Crustal stress pattern across scales. Tectonophysics 744, 484–498.

Jackson, J., 1980. Reactivation of basement faults and crustal shortening in orogenic belts. Nature 283, 343–346.

Jackson, J., 1992. Partitioning of strike-slip and convergent motion between Eurasia and Arabia in eastern Turkey and the Caucasus. J. Geophys. Res. Solid Earth 97, 12471–12479.

Jackson, J., Fitch, T., 1981. Basement faulting and the focal depths of the larger earthquakes in the Zagros mountains (Iran). Geophys. J. Int. 64, 561–586.

Jackson, J., McKenzie, D., 1984. Active tectonics of the Alpine—Himalayan Belt between western Turkey and Pakistan. Geophys. J. Int. 77, 185–264.

Khorrami, F., Vernant, P., Masson, F., Nilfouroushan, F., Mousavi, Z., Nankali, H., Saadat, S.A., Walpersdorf, A., Hosseini, S., Tavakoli, P., 2019. An up-to-date crustal deformation map of Iran using integrated campaign-mode and permanent GPS velocities. Geophys. J. Int. 217, 832–843.

Koshnaw, R.I., Schlunegger, F., Stockli, D.F., 2021. Detrital zircon provenance record of the Zagros mountain building from the Neotethys obduction to the Arabia-Eurasia collision, NW Zagros fold-thrust belt, Kurdistan region of Iraq. Solid Earth Discuss. 1–33.

Lee, J.-C., Angelier, J., 1994. Paleostress trajectory maps based on the results of local determinations: the "Lissage" program. Comput. Geosci. 20, 161–191.

Levandowski, W., Herrmann, R.B., Briggs, R., Boyd, O., Gold, R., 2018. An updated stress map of the continental United States reveals heterogeneous intraplate stress. Nat. Geosci. 11, 433–437.

Lund, B., Townend, J., 2007. Calculating horizontal stress orientations with full or partial knowledge of the tectonic stress tensor. Geophys. J. Int. 170, 1328–1335.

Martínez-Garzón, P., Ben-Zion, Y., Abolfathian, N., Kwiatek, G., Bohnhoff, M., 2016. A refined methodology for stress inversions of earthquake focal mechanisms. J. Geophys. Res. Solid Earth 121, 8666–8687.

McQuarrie, N., 2004. Crustal scale geometry of the Zagros fold–thrust belt Iran. J. Struct. Geol. 26, 519–535.

McQuarrie, N., Stock, J., Verdel, C., Wernicke, B., 2003. Cenozoic evolution of Neotethys and implications for the causes of plate motions. Geophys. Res. Lett. 30.

Michael, A.J., 1987. Use of focal mechanisms to determine stress: a control study. J. Geophys. Res. Solid Earth 92, 357–368.

Michael, A.J., 1991. Spatial variations in stress within the 1987 Whittier Narrows, California, aftershock sequence: New techniques and results. J. Geophys. Res. Solid Earth 96, 6303–6319.

Michael, A.J., Ellsworth, W.L., Oppenheimer, D.H., 1990. Coseismic stress changes induced by the 1989 Loma Prieta, California earthquake. Geophys. Res. Lett. 17, 1441–1444.

Navabpour, P., Angelier, J., Barrier, E., 2008. Stress state reconstruction of oblique collision and evolution of deformation partitioning in W-Zagros (Iran, Kermanshah). Geophys. J. Int. 175, 755–782.

Niassarifard, M., Shabanian, E., Azad, S.S., Madanipour, S., 2021. New tectonic configuration in NW Iran: Intracontinental dextral shear between NW Iran and SE Anatolia. Tectonophysics 811, 228886.

Nissen, E., Ghorashi, M., Jackson, J., Parsons, B., Talebian, M., 2007. The 2005 Qeshm Island earthquake (Iran)—a link between buried reverse faulting and surface folding in the Zagros simply folded belt? Geophys. J. Int. 171, 326–338.

Nissen, E., Ghods, A., Karasözen, E., Elliott, J.R., Barnhart, W.D., Bergman, E.A., Hayes, G.P., Jamal-Reyhani, M., Nemati, M., Tan, F., 2019. The 12 November 2017 M w 7.3 Ezgeleh-Sarpolzahab (Iran) earthquake and active tectonics of the Lurestan Arc. J. Geophys. Res. Solid Earth 124, 2124–2152.

Nouri Mokhoori, A., Rahimi, B., Moayyed, M., 2021. Active tectonic stress field analysis in NW Iran-SE Turkey using earthquake focal mechanism data. Turk. J. Earth Sci. 30, 235–246.

Pascal, C., 2021. Paleostress Inversion Techniques: Methods and Applications for Tectonics. Elsevier, 265 p.

Pourbeyranvand, S., 2018. Stress studies in the Central Alborz by inversion of earthquake focal mechanism data. Acta Geophysica 66, 1273–1290.

Ranjbar-Karami, R., Rajabi, M., Ghavidel, A., Afroogh, A., 2019. Contemporary tectonic stress pattern of the Persian Gulf Basin, Iran. Tectonophysics 766, 219–231.

Reasenberg, P., 1985. Second-order moment of Central California seismicity, 1969–1982. J. Geophys. Res. Solid Earth 90, 5479–5495.

Rebetsky, Y.L., Lukk, A., Tatevossian, R., Bykova, V., 2017. Determination of weak earthquake focal mechanisms and modern geodynamics of southern Iran. Geodyn. Tect. 8, 971–988.

Reilinger, R., McClusky, S., Vernant, P., Lawrence, S., Ergintav, S., Cakmak, R., Ozener, H., Kadirov, F., Guliev, I., Stepanyan, R., 2006. GPS constraints on continental deformation in the Africa-Arabia-Eurasia continental collision zone and implications for the dynamics of plate interactions. J. Geophys. Res. Solid Earth 111.

Roustaei, M., Nissen, E., Abbassi, M., Gholamzadeh, A., Ghorashi, M., Tatar, M., Yamini-Fard, F., Bergman, E., Jackson, J., Parsons, B., 2010. The 2006 March 25 Fin earthquakes (Iran)—insights into the vertical extents of faulting in the Zagros Simply Folded Belt. Geophys. J. Int. 181, 1275–1291.

Sarkarinejad, K., Zafarmand, B., Oveisi, B., 2018. Evolution of the stress fields in the Zagros Foreland Folded Belt using focal mechanisms and kinematic analyses: the case of the Fars salient Iran. Int. J. Earth Sci. 107, 611–633.

Scholz, C.H., 2019. The Mechanics of Earthquakes and Faulting. Cambridge university press, Cambridge, p. 493.
Simpson, R.W., 1997. Quantifying Anderson's fault types. J. Geophys. Res. Solid Earth 102, 17909–17919.
Snee, J.-E.L., Zoback, M.D., 2020. Multiscale variations of the crustal stress field throughout North America. Nat. Commun. 11, 1–9.
Soh, I., Chang, C., Lee, J., Hong, T.-K., Park, E.-S., 2018. Tectonic stress orientations and magnitudes, and friction of faults, deduced from earthquake focal mechanism inversions over the Korean Peninsula. Geophys. J. Int. 213, 1360–1373.
Stein, R.S., 1999. The role of stress transfer in earthquake occurrence. Nature 402, 605–609.
Stern, R.J., Moghadam, H.S., Pirouz, M., Mooney, W., 2021. The Geodynamic Evolution of Iran. Annu. Rev. Earth Planet. Sci. 49, 9–36.
Talebian, M., Jackson, J., 2002. Offset on the Main Recent Fault of NW Iran and implications for the late Cenozoic tectonics of the Arabia–Eurasia collision zone. Geophys. J. Int. 150, 422–439.
Talebian, M., Jackson, J., 2004. A reappraisal of earthquake focal mechanisms and active shortening in the Zagros mountains of Iran. Geophys. J. Int. 156, 506–526.
Tavakoli, F., Walpersdorf, A., Authemayou, C., Nankali, H., Hatzfeld, D., Tatar, M., Djamour, Y., Nilforoushan, F., Cotte, N., 2008. Distribution of the right-lateral strike–slip motion from the main recent Fault to the Kazerun Fault System (Zagros, Iran): evidence from present-day GPS velocities. Earth Planet. Sci. Lett. 275, 342–347.
Townend, J., Sherburn, S., Arnold, R., Boese, C., Woods, L., 2012. Three-dimensional variations in present-day tectonic stress along the Australia–Pacific plate boundary in New Zealand. Earth Planet. Sci. Lett. 353, 47–59.
Vavryčuk, V., 2011. Principal earthquakes: Theory and observations from the 2008 West Bohemia swarm. Earth Planet. Sci. Lett. 305, 290–296.
Vavryčuk, V., 2014. Iterative joint inversion for stress and fault orientations from focal mechanisms. Geophys. J. Int. 199, 69–77.
Vavryčuk, V., 2015. In: Beer, M., Kougioumtzoglou, I., Patelli, E., Au, I. (Eds.), Earthquake mechanisms and stress field. In: Encyclopedia of earthquake engineering, pp. 728–746.
Vavryčuk, V., Bouchaala, F., Fischer, T., 2013. High-resolution fault image from accurate locations and focal mechanisms of the 2008 swarm earthquakes in West Bohemia, Czech Republic. Tectonophysics 590, 189–195.
Vernant, P., Chéry, J., 2006. Mechanical modelling of oblique convergence in the Zagros, Iran. Geophys. J. Int. 165, 991–1002.
Vernant, P., Nilforoushan, F., Hatzfeld, D., Abbassi, M., Vigny, C., Masson, F., Nankali, H., Martinod, J., Ashtiani, A., Bayer, R., Tavakoli, F., Chery, J., 2004. Present-day crustal deformation and plate kinematics in the Middle East constrained by GPS measurements in Iran and northern Oman. Geophys. J. Int. 157, 381–398.
Walpersdorf, A., Hatzfeld, D., Nankali, H., Tavakoli, F., Nilforoushan, F., Tatar, M., Vernant, P., Chéry, J., Masson, F., 2006. Difference in the GPS deformation pattern of North and Central Zagros (Iran). Geophys. J. Int. 167, 1077–1088.
Zebari, M., Preusser, F., Grützner, C., Navabpour, P., Ustaszewski, K., 2021. Late pleistocene-holocene slip rates in the Northwestern Zagros Mountains (Kurdistan Region of Iraq) derived from luminescence dating of river terraces and structural modeling. Tectonics 40 e2020TC006565.
Zoback, M.L., 1992. First-and second-order patterns of stress in the lithosphere: the world stress map project. J. Geophys. Res. Solid Earth 97, 11703–11728.